Inorganic Chemistry

Article

pubs.acs.org/IC

Nanocomposite $YCrO_3/Al_2O_3$: Characterization of the Core–Shell, Magnetic Properties, and Enhancement of Dielectric Properties

A. Durán,*[,†] H. Tiznado,[†] J. M. Romo-Herrera,[†] D. Domínguez,[†] R. Escudero,[‡] and J. M. Siqueiros[†]

[†]Universidad Nacional Autónoma de México, Centro de Nanociencias y Nanotecnología, Km. 107 Carretera Tijuana-Ensenada, Apartado Postal 14, C. P. 22800, Ensenada, B. C. México

[‡]Universidad Nacional Autónoma de México, Instituto de Investigaciones en Materiales, Apartado Postal 70-360, México, D. F. 04510, México

ABSTRACT: Multifuncionality in polycrystalline multiferroic ceramics can be improved using an advanced synthesis process. In this work, core–shell design is being proposed to enhance the transport properties of biferroic $YCrO_3$. The atomic layer deposition (ALD) thin-film growth technique was used for the $YCrO_3/Al_2O_3$ (Y@Al) nanocomposite fabrication. A continuous, amorphous, and uniform Al_2O_3 shell, a few nanometers thick, was obtained and characterized by X-ray photoelectron spectroscopy, X-ray diffraction, and high-resolution transmission electron microscopy. The transport properties of biferroic $YCrO_3$ coated with 50, 500, and 1000 ALD cycles of insulating Al_2O_3 were investigated using magnetization and AC conductivity measurements. It is observed that the values of the magnetic coercive field and the magnetization are affected by the amorphous and partially crystallized Al_2O_3 shell. Additionally, the Y@Al nanocomposite experiments show a notorious decreasing in the loss tangent and the electrical conductivity. Accordingly, hysteresis loops in the polarization versus electric energy data confirm the decrease of the leakage current as a consequence of the Al_2O_3 shell acting as a barrier layer. The results shown here confirm that the core–shell architecture is a promising alternative for improvement of the magnetic and ferroelectric properties in bulk multiferroics.

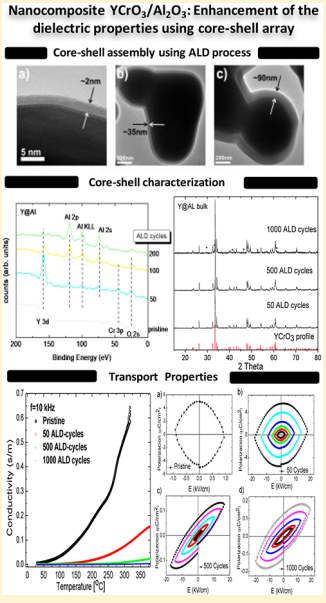

INTRODUCTION

Nanocomposite ceramics have received significant scientific and technological attention over the past several decades. Nano-coated particles are an entirely new class of materials, showing considerable potential for new applications.[1−6] In recent years, significant effort has been devoted to the design and controlled fabrication of nanostructured materials with functional properties. The core–shell architecture is an effective approach to build tailored nanomaterials of great importance from both fundamental and applied points of view.[7−9] Core–shell particles often exhibit very different physical and chemical properties than their single-component counterparts. Ferroelectric core–shell array is a promising architecture for the fabrication of functional bulk composites that can potentially be used as dielectric resonators, supercapacitors, or multiferroic-based devices.[10−13] The shell covering the ferroelectric core acts as barrier layer confining electronic and ionic space charges, increasing thus the capacitance density.[11,14] In multiferroics, their inherent semiconducting character reduces the ferroelectric and piezoelectric response mainly due to the partially filled d-orbitals. In bulk multiferroics, the applied electric field moves the electronic and ionic space charges through the grain/particles boundaries affecting, significantly, the ferroelectric properties. In this regard, the core–shell array seems to be a good alternative to improve the ferroelectric properties. Thus, the insulating oxide coating on each multiferroic particle acts as barrier layer improving the interface boundaries of the particles and leading to an increased functionality, that is, higher charge storage and lower dielectric losses. In $YCrO_3$, the large dielectric losses and the changes of the conduction activation energy have been shown to be very dependent on the synthesis route as well as on the size and chemical state of the starting grains.[15,16] The increase of the conductivity and the dielectric losses are associated with free charges leaking out through the grain/particles boundary. Recent studies by electron-beam induced current (EBIC) in $YCrO_3$ thin films found charge accumulation at the grain boundary. The charge accumulation diminishes with film thickness as a consequence of grain coalescence and the decrease of grain boundaries.[17] Nanocomposite alumina-based $YCrO_3$ ceramics may overcome this shortcoming. Alumina is the most widely used ceramic oxide; it has good dielectric properties with high dielectric constant, good gate leakage, and

Received: November 29, 2013
Published: May 8, 2014

   dx.doi.org/10.1021/ic4029589 | *Inorg. Chem.* 2014, 53, 4872−4880

very good thermal and chemical stability.[18−20] Thus, the insulating Al_2O_3 shell covering the particles acts as a barrier layer confining and/or localizing the free charges within the particles, improving thus the magnetic and dielectric properties.

In this work we study the magnetic and electric properties of the Y@Al core−shell nanocomposite. The atomic layer deposition (ALD) technique was employed to coat the $YCrO_3$ with a ∼3, 30, or 90 nm thick Al_2O_3 shell, followed by annealing and a sintering step to construct the Y@Al multiferroic capacitor. After each step of the process, the samples were carefully characterized by XPS, XRD, SEM, and HRTEM, and finally, the magnetic and dielectric properties were obtained. The results show that the amorphous and partial crystallization of the Al_2O_3 shell have an effect on the magnetic hysteresis features. Furthermore, the Al_2O_3 shell acts as a barrier layer localizing the charge carriers, improving thus the ferroelectric characteristics. Here, we show that bulk magnetic and ferroelectric properties can be improved by means of controlled layer growth of an insulating Al_2O_3 shell in the biferroic $YCrO_3$.

EXPERIMENTAL DETAILS

The combustion method was used to produce polycrystalline samples. Stoichiometric amounts of precursor nitrates $Y(NO_3)_3{\cdot}5H_2O$ (99.99% Alfa-Aesar) and $Cr(NO_3)_3{\cdot}9H_2O$ (99.9% Sigma-Aldrich) as well as 2-methoxyethanol acting as both solvent and carburant were mixed at a ratio of 10 mL of carburant per gram of desired product. More experimental details about the preparation method have been given elsewhere.[16] The crystalline particles were ground and then dispersed using an ultrasonic probe. The ALD route was used to deposit the Al_2O_3 coating on the $YCrO_3$ powders particles, producing the core−shell $YCrO_3/Al_2O_3$ nanocomposite architecture. Trimethylaluminum (TMA) was used as aluminum precursor, and H_2O was used as the oxygen source. The TMA vapors were injected into the nitrogen (N_2) carrier gas using pulsed valves and transported to the sample powders. Two half-reactions occur at the particle surface. The self chemical absorption of TMA is the first one. Here, the sample is exposed to TMA long enough to saturate the powder surface. The second half-reaction is aimed to oxidize the TMA absorbed using water vapor forming Al−O linkages. These two half-reactions complete one ALD cycle, which typically results in a coverage of less than a layer of Al_2O_3 on the powder surface and thus regenerates the original starting surface so that the process can be repeated. In this way, it is possible to grow Al_2O_3 coatings from one layer thickness to tens of nanometers. More details of the ALD process are described elsewhere.[21] Complete coatings of the particles were carried out with 50, 500, and 1000 repetitive cycles. After this, the Y@Al particles were heat-treated (HT) in air at 1200 °C for 2 h using a heating rate of 1 °C min^{-1}. The surface chemical analysis of the powder samples fixed on vacuum-compatible carbon tape from SPI was carried out using X-ray photoelectron spectroscopy (XPS). Low-resolution (200 eV pass energy) analyses were taken with a Leybold LH18 system at a pressure below 1×10^{-9} Torr. The system is equipped with a hemispherical electron analyzer model LH10 and a dual anode X-ray source model Specs XRC 1000; the Mg Kα line at 1253.6 eV was used. The binding energy (BE) of the C 1s peak at 284.5 eV was taken as the internal standard for charge-induced shifting correction. The identification of the crystalline phase was made with a conventional powder X-ray diffractometer using a Cu Kα radiation (λ = 0.154 18 nm). Data were collected in the range of $10° < 2\theta < 90°$ with 0.02° step scan. The microstructural characterization of the powders was performed using high-resolution transmission electron microscopy (HTREM). TEM micrographs of the samples were obtained with a JEOL JEM 2010 operating at 200 kV. The elemental analysis was performed by energy-dispersive X-ray spectrometry (EDX) in the column detector of a JEOL JEM 2100F, with the microscope operating at 200 kV in scanning transmission electron microscopy (STEM) mode. Determination of the bulk Y@Al morphology and the EDX analysis were carried out using a JEOL (JSM-5300) scanning electron microscope (SEM). Magnetization was measured with a SQUID-based magnetometer MPMS-5T (Quantum Design). The electrical properties were evaluated in bulk pellets. The Y@Al HT powders were compacted, in a cylindrical die with a diameter of 6 mm, at ∼1 Ton of uniaxial pressure. Then, the samples were sintered as follows: cold-pressed pellets were placed in alumina (99.9%) plate crucibles and heated at a rate of 3 °C min^{-1} to 1200 °C and kept there for 2 h. Afterward, the samples were sintered at 1350 °C, raising the temperature at a rate of 5 °C min^{-1} for another 2 h, and then cooled to room temperature (at 15 °C min^{-1}). The sintered pellets (6 × 1.2 mm) were finally coated with conductive silver paint, dried at 500 °C for 1 min, and cooled to room temperature. The electric features of the samples were measured with an LCR (HP 4284 A) bridge from 1 kHz to 50 kHz. The polarization-electric field (P-E) curves were obtained with an RT66A ferroelectric tester by Radiant Technologies.

RESULTS AND DISCUSSION

(a). Chemical Analysis and Microstructural Characterization after the ALD Process and Heat Treatment at 1200 °C of the Nanocomposite Y@Al Powders.

Figure 1 shows the XPS spectra acquired after several accumulative ALD cycles. The spectrum for the pristine $YCrO_3$ sample shows the corresponding Y 3d, Cr 3p, and O 2s peaks. Then, as the number of ALD cycles adds up, the intensity of these peaks decreases, while peaks for Al 2p, 2s, and Al KLL Auger transition for Al_2O_3 increase in intensity. After 200 cycles, no peaks for Y and Cr are detected, indicating that the Al_2O_3 layer thickness is larger than the Y and Cr photoelectron escape depth. The O 2s peak looks very similar along the process as is common for both oxides. This result demonstrates that the Al_2O_3 is growing on top of $YCrO_3$ powders with a high degree of thickness control.

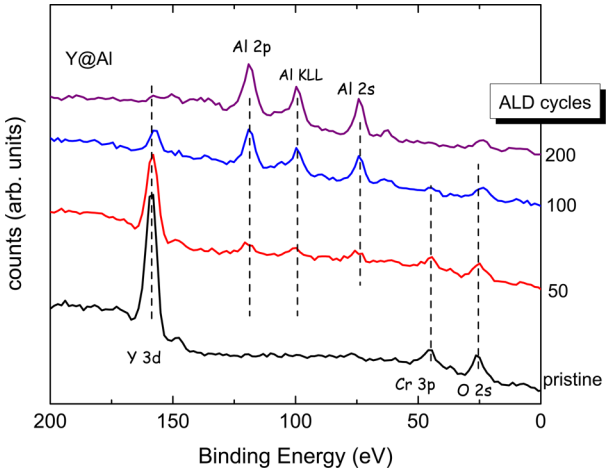

Figure 1. Series of XPS spectra showing the evolution of the Al_2O_3 ALD coating on the $YCrO_3$ powder for pristine, 50, 100, and 200 cycles.

As expected, the core−shell arrangements for 50, 500, and 1000 ALD cycles were confirmed from microstructural analysis. Figure 2a shows one of the $YCrO_3$ particles coated with 50 ALD cycles of Al_2O_3. The dark field image shows the Al_2O_3-shell interface (gray interface) around the $YCrO_3$ core (light zone). A grain with uniform ∼3 nm thick coating is clearly observed (site 1 in Figure 2). Elemental composition was examined by EDX analysis using TEM in STEM mode. The EDX spectra from three different sites, marked by circles in

dx.doi.org/10.1021/ic4029589 | Inorg. Chem. 2014, 53, 4872−4880

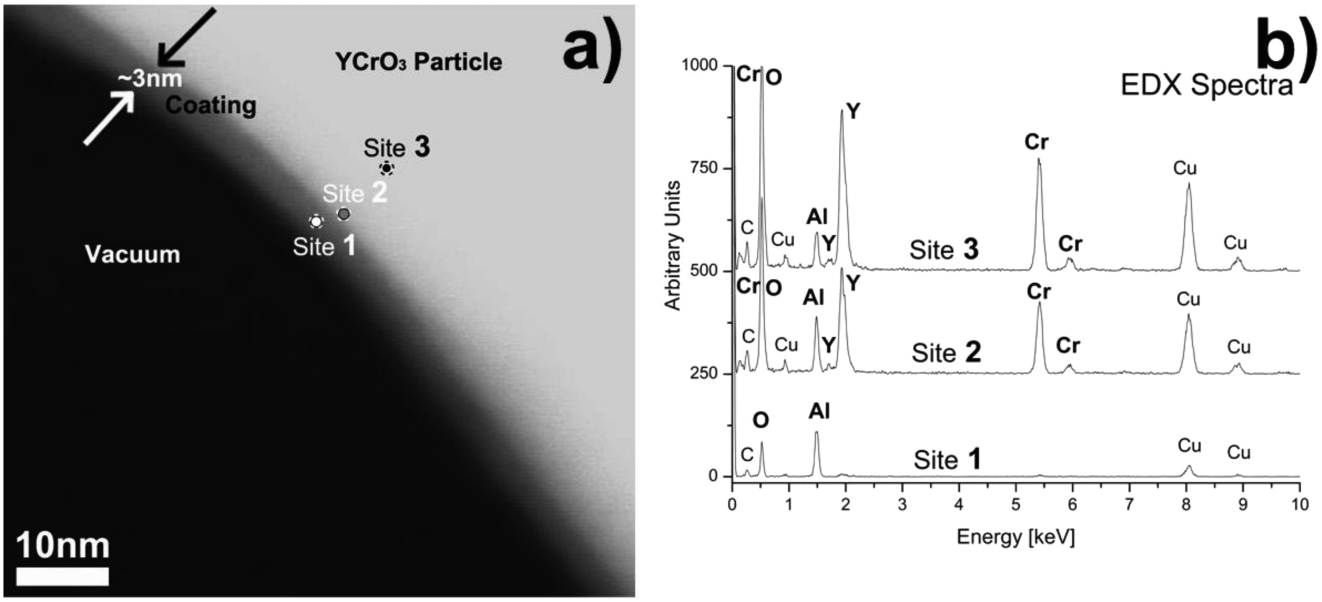

Figure 2. (a) TEM dark field image showing a gray interface at the boundary of the grain. The arrows mark the thickness of about 3 nm. (b) EDX analysis confirms that the gray interface corresponds to Al_2O_3 (site 1). At site 2 the Y and Cr signals start appearing, and finally, at site 3, the Y and Cr signals appear from the core; Al signal from the core surface is observed.

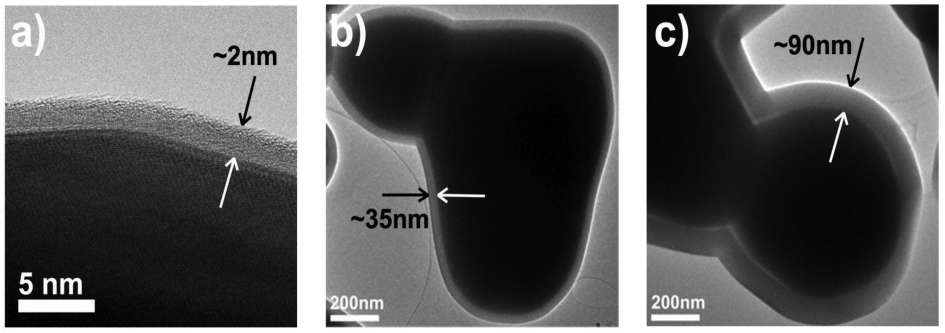

Figure 3. TEM images showing the Y@AL core−shell structure. The images display good distribution and homogeneity of the Al_2O_3 shell (gray coating) around the core grains. The arrows at the edges of the Y@Al nanocomposite indicate the thickness of the Al_2O_3 shell of about 2 nm (a), 35 nm (b), and 90 nm (c), corresponding to 50, 500, and 1000 ALD cycles, respectively.

Figure 2a, are shown in Figure 2b. The first EDX spectrum corresponds to the gray interface (site 1, marked in Figure 2a), showing the Al and O presence at about 1.48 and 0.48 keV [Kα], respectively. The spectra from sites two and three show peaks of Cr and Y around of 5.41 and 1.92 keV [Kα] along with the Al peak. Copper and carbon signals belong to the TEM grid. This elemental analysis shows that the particles are completely covered with Al_2O_3, confirming the Y@Al core−shell array expected. TEM analysis of the particles covered with 50, 500, and 1000 ALD cycles revealed thicknesses of about 2−3, 35, and 90 nm, respectively, as is displayed by the representative micrographs in Figure 3a−c. These thicknesses indicate that the growth rate gives an average of about 0.73 Å per cycle. This value is lower than that reported (using TMA precursor) for thin-film growth on Si substrate in other reports.[21,22] It is worth noting that the ALD process allows the uniform and homogeneous coverage with Al_2O_3 on the sharp corners and rounded edges of each particle as seen in Figure 3c.

To consolidate and induce crystallization of the Al_2O_3 shell at the surface of the core, the Y@Al core−shell powders were annealed at 1200 °C. X-ray diffraction was performed to confirm possible crystallization of the coating or the formation of second phases between the coating and the $YCrO_3$ particles during heat treatment. Figure 4 shows the X-ray diffraction for the uncoated, after the 500-ALD process, and HT at 1200 °C (coated with 500 ALD cycles) samples. A direct comparison shows a single $YCrO_3$ crystalline phase in the Y@Al structure. The absence of extra peaks suggests that no extra phases are present even in the 1200 °C HT sample. It is also observed that the relative intensity of the $YCrO_3$ peaks is slightly attenuated as the coating thickness increases.

To confirm a possible Al_2O_3-shell crystallization, a more focused inspection by HRTEM analysis was performed in the sample coated with 1000 ALD cycles, as is presented in Figure 5a−d. A gray interface is observed at the edge of the grains, indicating that the particles are still very well-covered with Al_2O_3 after heat treatment. The aspect of the surface is rough with typical "orange skin" appearance at the edge of the gray interface (arrows in Figure 5a,b). Note that the coating thickness was reduced from ~90 to ~70 nm, corresponding to shrinkage of around 20%, as is indicated (white arrows) in Figure 5a,c. The shrinkage and surface morphology changes are due to the dehydration and dehydroxylation during the heat treatment process, leading to an increase of the coating

dx.doi.org/10.1021/ic4029589 | Inorg. Chem. 2014, 53, 4872−4880

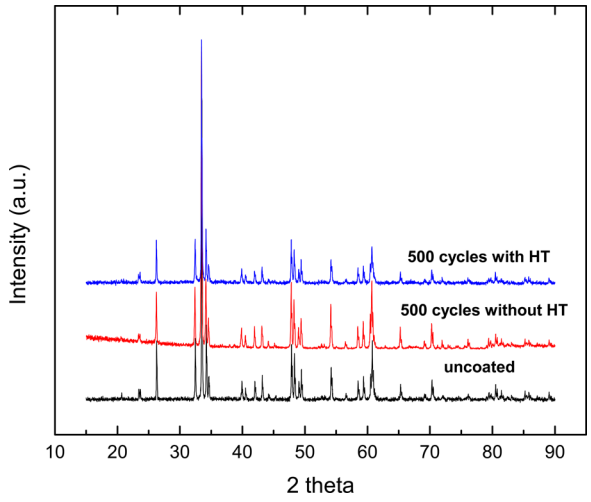

Figure 4. X-ray diffraction patterns for uncoated, 500 ALD cycles without heat treatment (TT), and 500 ALD cycles with heat treatment. All diffraction peaks are indexed with single $YCrO_3$ phase.

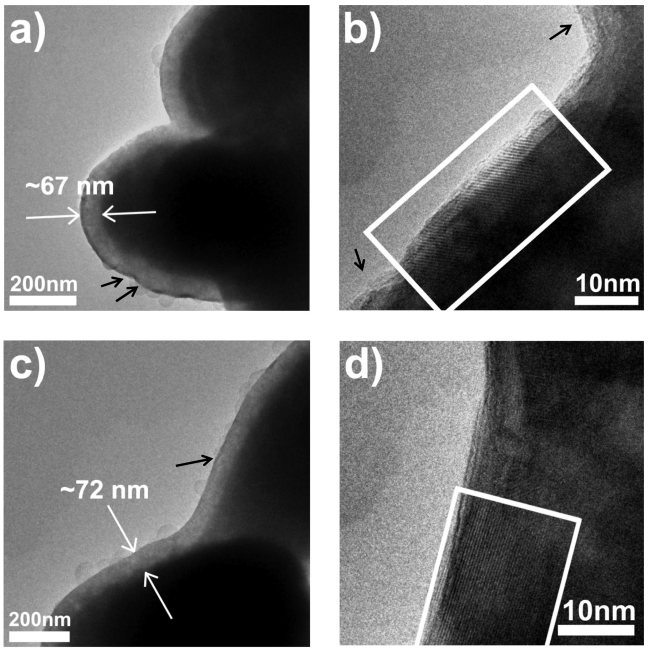

Figure 5. TEM images of coated particles (1000 ALD cycles) HT at 1200 °C. The gray interface of about 67 and 72 nm of two different particles is shown as white arrows in (a) and (c). Amplifications from images (a) and (c) are presented in (b) and (d), respectively. The white rectangles in (b) and (d) indicate small crystalline domains along the coating layer. Black arrows indicate the rough surface.

density.[24,26−28] It has often been reported that for two half-reactions of TMA on thin films and particles, the resulting aluminum oxide consists of Al atoms linked with oxygen, as well as some hydroxyls, water, and carboxyl molecules in an amorphous network.[22−25] Figure 5b displays a zoom of the coating particles shown in Figure 5a. In the micrograph, small crystalline domains (marked with a white rectangle) can be seen, and they are evidence of partial crystallization after the heat treatment. Similarly, Figure 5d presents a magnification of the coating of the particle shown in Figure 4c. Also, small crystalline zones (within the white rectangle) on the order of 15−30 nm can be seen. It is worth noting the lack of complete crystallization of the Al_2O_3 coating at 1200 °C. This behavior is opposite to that observed in nanometric powders, thin films, and core−shell structures. For instance, S. Cava et al.[29] found that the amorphous and the nanometric-sized powders (~55 nm) lead to low metastable Al_2O_3 crystallization at 800 °C. In thin films,[25] a strong and well-defined XRD peak of α-Al_2O_3 has been observed after a postannealing treatment (1150 °C). However, it should be emphasized that different Al_2O_3 crystallization mechanisms occur in the core−shell assembly process. Besides the postannealing temperature, other factors such as type of amorphous/polycrystalline shell array, distribution and scale of surface inhomogeneities (defects, second phases), interdiffusion, and chemical reactivity at interface, as well as the melting point of the core and shell, are some important parameters that affect the crystallization in these structures. In particles coated with insulating silica and alumina-shell, perhaps the most unusual behavior was observed in this study. Despite the limited experimental studies of the diffusion mechanism at interface in the particles coated with Al_2O_3, here, we suggest three main factors that could hinder the crystallization of the Al_2O_3 shell at 1200 °C: (i) the high chemical and structural stability at high temperature of the $YCrO_3$ ceramic core compound, (ii) the low reactivity at the interface between Y−O, Cr−O, and Al−O groups, and (iii) the core-particle size (>500 nm). The sum of these factors could inhibit the crystallization of the amorphous Al_2O_3 shell at the postannealing temperature (1200 °C). It is well-known that the Y−O and Cr−O covalent bonds grant high chemical stability, leading to a high melting point (~2200 °C).[30,31] This condition could delay the full or metastable crystallization of the Al_2O_3 shell as well as the interdiffusion mechanism across the Y@Al interface. Nevertheless, the partial crystallization does not stay at the sintering temperature, as discussed below. In view of the shrinkage of the Al_2O_3 shell after the heat treatment, henceforth, the nanocomposites samples will be referred as 50, 500, and 1000 cycles.

(b). Characterization of the Sintered Y@AL Pellets. Figure 6 shows the SEM micrographs of the surface (a, b) and cross-section fracture (c) of the bulk Y@Al nanocomposite. Figure 6a,b shows, at two different magnifications, elongated grains and some porosity indicating that a complete densification in the bulk has not been achieved at 1350 °C. Figure 6c,d shows the micrographs of the cross-section fracture and the EDX spectrum. The spectrum reveals peaks of Cr and Y along with Al peaks around 1.48 keV. This analysis indicates the presence of Al in the bulks. A question to be answered is whether the Al_2O_3 shell is crystallized in the sintered Y@AL samples. To clarify this matter, X-ray diffraction was performed on the bulk, as is seen in Figure 7. No extra peaks were indexed in the 50 and 500 ALD-cycle samples. However, a second phase was easily detected in the 1000 ALD-cycle bulk, as seen in the top X-ray pattern of Figure 7. This phase was indexed as $Y_3Al_5O_{12}$ (JCPDS 79−1891) or YAG phase. Thus, we should not rule out a weak signal of X-ray diffraction from the nanolayer of YAG phase, which can be confused with the background for the 50 and 500 ALD-cycle samples. Note that the shell does not crystallize in α-Al_2O_3. Here, it is clear that the high temperature induces a diffusion process leading to the crystallization from the core to the shell to form a new YAG phase. This diffusion mechanism is not an isolated process. Recently, a deeper microstructural study in $BaTiO_3$@SiO_2 core−shell showed that the diffusion process is activated from the Ba core to the Si shell to form fresnoite ($Ba_2TiSi_2O_8$) at the

dx.doi.org/10.1021/ic4029589 | Inorg. Chem. 2014, 53, 4872−4880

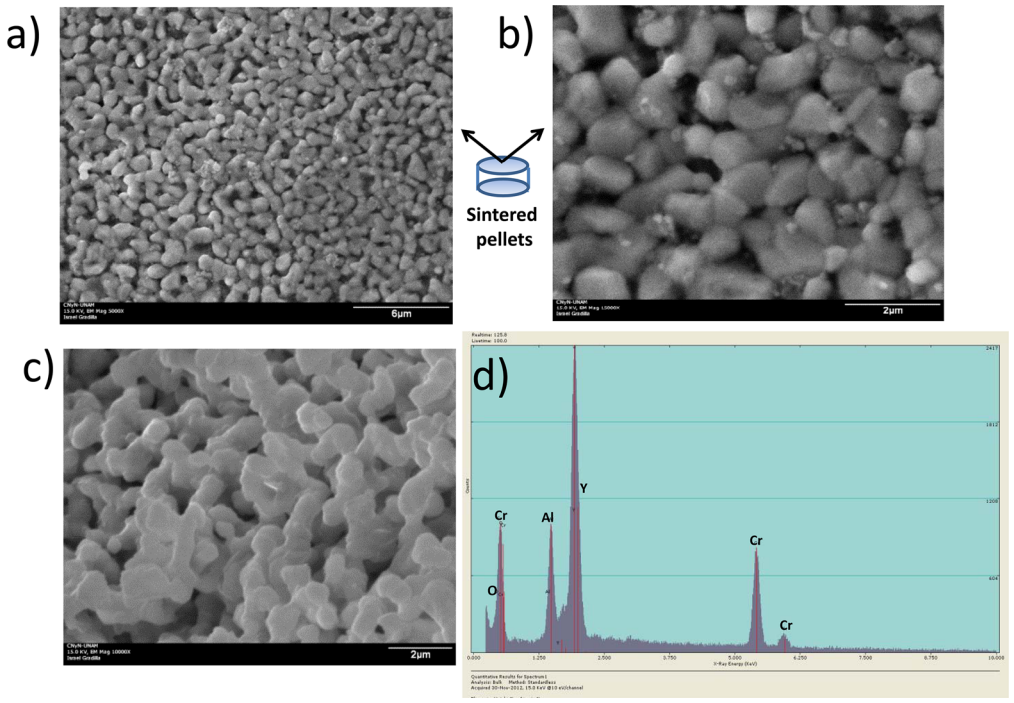

Figure 6. SEM images showing the morphology of the sintered bulk sample. (a) and (b) display the surface, at two magnifications, of the Y@Al sintered bulk. The (c) and (d) images shows the microstructure and the EDX analysis of the cross section of the Y@AL sintered bulk.

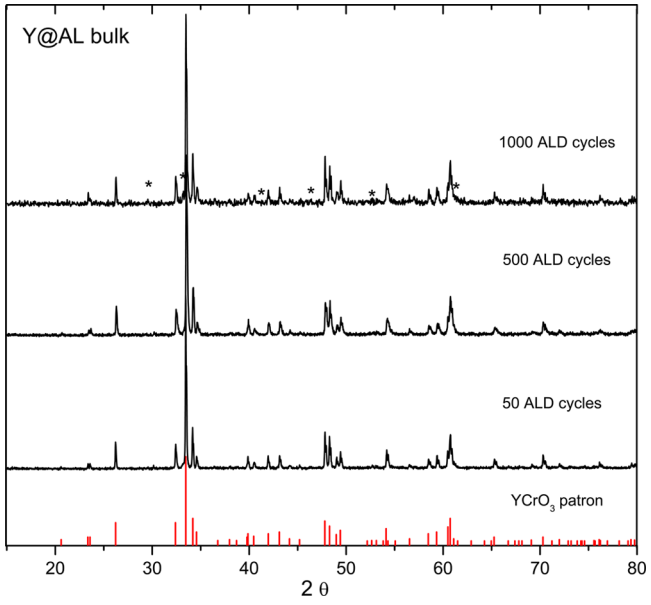

Figure 7. XRD profiles for 50, 500, and 1000 ALD cycles of the Y@Al sintered bulk. The bar pattern of the $YCrO_3$ is showed at the bottom for comparison. Asterisks mark the position of the weak second phase peaks indexed as $Y_3Al_5O_{12}$.

interface.[14] Also, in TiO_2@Al_2O_3 postannealing induces migration from the core to the Al_2O_3 shell to form aluminum titanate (Al_2TiO_5) at about 1280 °C.[32] In both works, the crystallization process occurs by diffusion from the core to the insulating shell with new phase crystallization. Nevertheless, we believe that the crystallization and diffusion mechanism through Y@Al interfaces is an important issue that will be addressed in depth in future work.

(c). Magnetic Properties. The magnetic hysteresis of the nanocomposite after the ALD process (amorphous Al_2O_3 shell) in zero field cooled (ZFC) mode at 5 K is shown in Figure 8. There, the hysteresis curve for each nanocomposite is

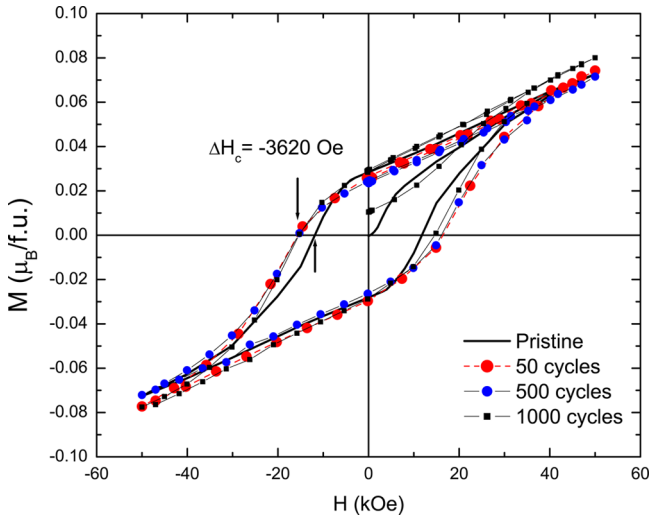

Figure 8. Magnetic hysteresis loop for 50, 500, and 1000 ALD-cycle samples (before any heat treatment) measured at 5 K for Y@Al. The pristine $YCrO_3$ sample hysteresis curve is included for comparison.

compared with that of the pristine sample. It should be stressed that the hysteresis loop of the pristine sample is due to the canted antiferromagnetic ordering of the Cr^{3+} (S = 3/2) occurring below ~140 K.[16,33] Note that the spin canting leads to a strong coercive field of about 1.19 kOe. Here, the magnetization is expressed in Bhor magneton per formula units, with the mass of the Al_2O_3 shell being included. It was found that the alumina shell affects the coercive field of the $YCrO_3$ core. The coercivity (H_c) is increased by about 3620 Oe for 50, 500, and 1000 cycles with respect to that of the pristine sample,

dx.doi.org/10.1021/ic4029589 | Inorg. Chem. 2014, 53, 4872−4880

as seen in Figure 8. Additionally, a slight increase of the unsaturated magnetization is observed at 50 kOe for the Y@Al with 1000 ALD cycles. It is evident that the coercive field increases after 50 ALD cycles, but after that, there are not appreciable changes for 500 and 1000 ALD cycles. The magnetic behavior in the Y@Al array is slightly different from that of other studies on magnetic cores with amorphous Al_2O_3 shell. The coercivity and magnetization is nearly independent of shell thickness, a fact that can be explained by assuming that the magnetic domains walls are pinned by particles wetting the surface with amorphous alumina, and, as a result, higher external magnetic force is required to have the domain walls fluctuating randomly with zero magnetization. Thus, the above statement implies that the H_c magnitude should be unchanged with the increase of shell thickness once the particle surface has been coated with Al_2O_3. Furthermore, a negligible increase of the magnetization in the 90 nm shell thickness particles implies that the spins tend to remain in their bulk configuration at 50 kOe. For instance, in $FeNi_3/Al_2O_3$ nanocomposite, the coercive field increases after $FeNi_3$ particles were coated with alumina, but the magnetization decreased slightly with an increase in alumina content.[34] Also, a strong dependence of the saturated magnetization with the shell thickness but without changes in the coercive field has been reported in $FeNi/SiO_2$ nanocomposite.[35]

On the other hand, an opposite trend is observed in the Y@Al HT samples. In Figure 9a the hysteresis curves for HT (1200 °C) coated samples are compared with that of the pristine sample. The H_c for the coated sample with 50 ALD cycles and the uncoated sample are practically equal. However, the coercivity decreased from 11.6 to 8.9 kOe for the $YCrO_3$ particles covered with 500 and 1000 ALD cycles. Furthermore, the unsaturated magnetization at 50 kOe increases gradually to 0.72, 0.85, and 0.11 μ_B/f.u. for the $YCrO_3$ covered with 50, 500, and 1000 ALD cycles, respectively. Figure 9b presents the Y@Al sample with 1000 ALD cycles without heat treatment together with the 50 and 1000 ALD-cycle particles, HT at 1200 °C. There, the effect of temperature in the coercive field and the unsaturated magnetization (50 kOe) is clearly observed. Recent studies have reported a strong temperature dependence of the coercivity and the saturation magnetization in several core−shell arrays.[36−38] For example, in the $Fe@SiO_2$ array, the saturation magnetization increased, whereas the coercivity decreased as the calcination temperature increased. These changes in the magnetization have been attributed to the exchange coupling across the Fe/Ferrihydrate interfaces.[36] However, in the present case, the most likely origin of the extra magnetic contribution could be found in the amorphous Al_2O_3 shell since the main source of the magnetic hysteresis loop comes from the $YCrO_3$ core. The crystalline α-Al_2O_3 does not have any magnetic moment; consequently, the bulk crystalline Al_2O_3 is diamagnetic. Recently, room-temperature ferromagnetic behavior has been reported in amorphous postannealed Al_2O_3 nanoparticles, indicating that the origin of ferromagnetism resides in the oxygen vacancies.[39,40] There, the disorder vacancies associated with structural disorder are the origin of the ferromagnetism behavior in amorphous insulating Al−O network. As Al−O amorphous network is crystallized by subsequent heat treatment, the strength of the exchange coupling (type-ferromagentic) decreases as a result of the structural order. Here, we speculate that at the same heat treatment temperature (1200 °C) where a partial crystallization of the Al_2O_3 shell is seen by TEM (see Figure 5), the oxygen

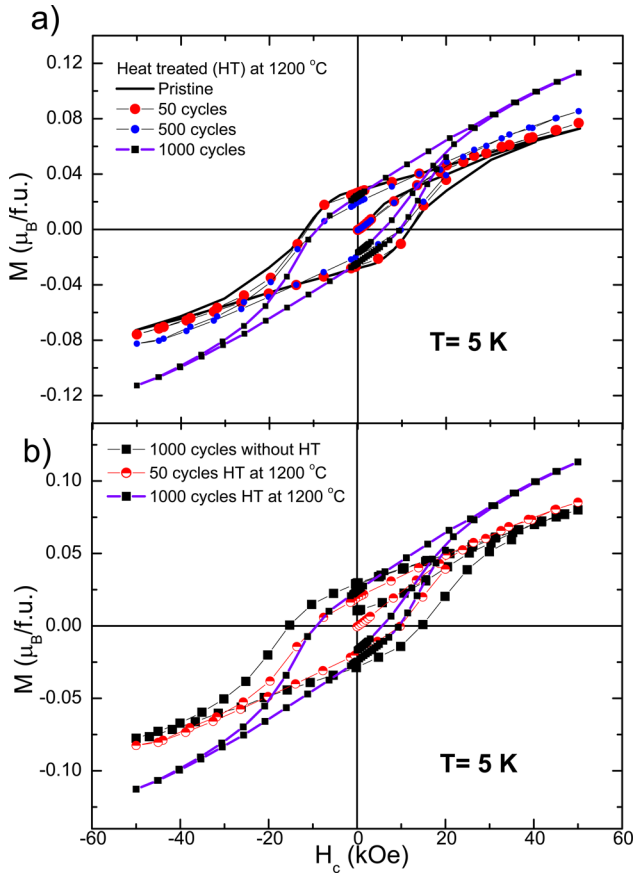

Figure 9. (a) Hysteresis loop for pristine, 50, 500, and 1000 ALD-cycle samples heat treated (HT) at 1200 °C. (b) Hysteresis loop for the Y@Al 1000 ALD cycle sample without HT, compared with the Y@Al 50 and 1000 ALD-cycle samples after HT at 1200 °C. Attention must be drawn to the effect of HT on the coercivity and the magnetization for 50 and 1000 ALD cycles of Al_2O_3 shell, indicating that the increase of ALD-shell thickness increases the exchange magnetic coupling across the Y@Al interface.

vacancy concentration must increase as the Al_2O_3 shell thickness increases, producing a higher magnetization. Such a scenario would explain the exchange coupling through the Y@Al interface and consequent increase the magnetization observed at 50 kOe. Thus, we believe that this is the source of the extra magnetic interaction that through the Y@Al interface gives rise to change in the hysteresis magnetic loops, as seen in Figure 9b. Accordingly, a magnetic component of the amorphous Al_2O_3 shell contributes (via exchange coupling) with the total magnetization of the Y@Al nanocomposite. However, further studies are needed to understand the exchange-coupling interaction in the Y@AL interface.

(d). Electrical Conductivity and Polarization. To explore the conductivity process in the uncoated and coated samples, the alternating current electrical conductivity (σ) was determined from the capacitance and dielectric loss (tan δ) versus temperature data at frequency of 10 kHz using the formula

$$\sigma_{\omega i}(T) = \frac{l}{s} \times \omega_i \times Cp_{\omega_i}(T) \times \tan \delta_{\omega_i} \quad (1)$$

where l is the thickness and s is the area of the electrode deposited on each nanocomposite sample. In Figure 10 the conductivity for the pristine and the Y@Al-coated samples with

dx.doi.org/10.1021/ic4029589 | Inorg. Chem. 2014, 53, 4872−4880

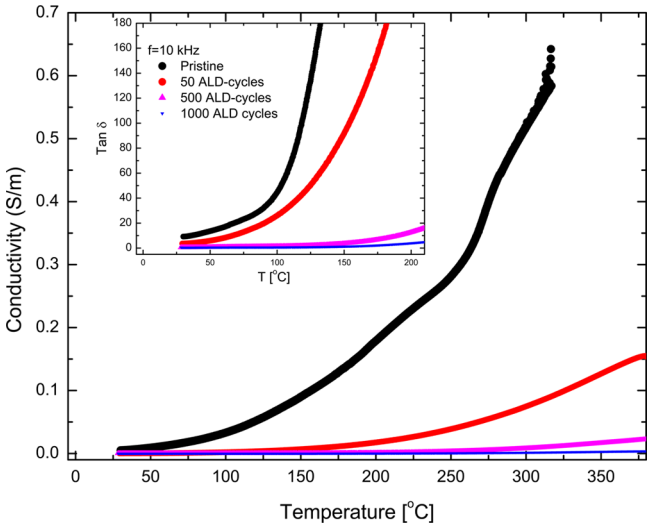

Figure 10. Temperature dependence of the conductivity for pristine, 50, 500, and 1000 ALD-cycle samples at 10 kHz. (inset) The loss tangent as a function of temperature.

50, 500, and 1000 cycles is compared. It is clearly observed that the electrical conductivity decreases when the coating thickness increases in the whole range of temperatures tested for Y@Al samples. A greater conductivity dispersion is observed in the uncoated sample than in the Y@Al samples above 150 °C. For example, the conductivity takes a value of about 0.18 S m^{-1} at 200 °C for the pristine sample, decreasing drastically to about 0.017, 9.10 × 10^{-4}, and 2.59 × 10^{-4} S m^{-1} for 50, 500, and 1000-cycle samples, respectively. Similar behavior was observed in the loss tangent (tan δ) as a function of temperature as seen in the inset of Figure 10. It is observed that the Y@Al samples show smaller tan δ in all range of temperature when compared with the pristine sample. Note that the Y@Al with 1000-cycle sample, in which tan δ takes values from 0.50 at room temperature to 6 at 220 °C, showed lower dispersion than that of an uncoated sample. It is well-known that, depending on the size and the chemical state of the starting grains, the sintering step of the bulk ceramic and its porosity can strongly alter the shape, the charges, and the electronic state of the grain boundaries. For $YCrO_3$, some discrepancies in the electrical properties have been observed, depending on the processing route.[15] Here, the decrease of the electrical conductivity and the

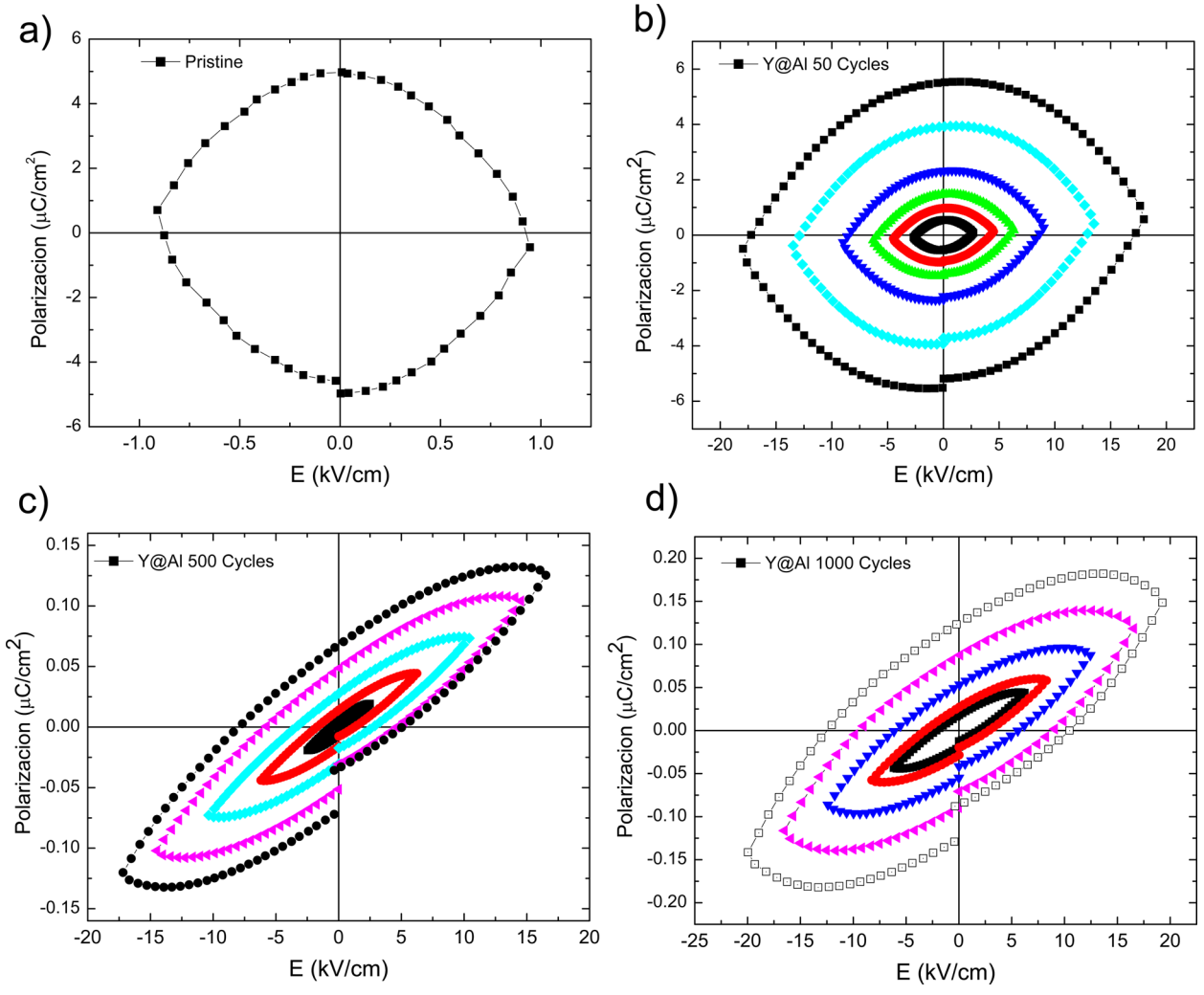

Figure 11. P-E hysteresis loops at room temperature and 1 kHz for nanocomposite Y@Al samples. (a) Pristine sample. For samples coated with Al_2O_3: (b) 50 ALD cycles, (c) 500 ALD cycles, and (d) 1000 ALD cycles. Clearly, the hysteresis loops gradually increase as the applied electric field is increased for the coated samples.

dx.doi.org/10.1021/ic4029589 | Inorg. Chem. 2014, 53, 4872−4880

dielectric loss can be nicely appreciated in the polarization hysteresis curve. It is well-known that, because of high conductivity, the observation of the hysteresis loop is very difficult, as, for instance, in bulk material $BiFeO_3$ (BFO).[41,42] In Figure 11, ferroelectric hysteresis loops were measured at 1 kHz for pristine, 50, 500, and 1000 ALD cycles of the Y@Al samples. For the pristine and the Y@Al coated with 50 ALD ALD-cycles rounded hysteresis loops are observed, characteristic of conductive ferroelectric material (see Figure 11a,b). Moreover, it is observed that the rounded hysteresis loops take high values (6 μC cm^{-2}) under applied electric field of 1 kV/cm^2 for pristine sample. For 50 Y@Al cycles, the round hysteresis loop is gradually increased, taking the same polarization values of the pristine sample but at higher applied electric field (~18 kV/cm^2). On the other hand, for 500 and 1000 ALD cycles the loops lose the rounded appearance, as seen in Figure 11c,d. It is interesting to note the change in shape of the hystresis loop with the increase of the Al_2O_3 layer on the $YCrO_3$ particles, which is due to the decrease of the electrical conductivity and the loss tangent, and thus decrease of the leakage current component. As a result, unsaturated polarization gradually increases as a function of applied electric field, taking values of about 0.15 and 0.20 μC cm^{-2} for 500 and 1000 ALD cycles. This behavior has been observed in other multiferroic materials.[42,43] For example, partial substitution of Fe ion by Ti ion in BFO films increased the direct current resistivity by more than 3 orders of magnitude, although Ti-doped BFO films did not exhibit saturated polarization.[43] On the other hand, C. L. Serrao et al.[44] showed rounded hysteresis loops at different temperatures in $YCrO_3$ films. M. P. Cruz et al.[17] showed that, by reducing the film thickness to several nanometers in $YCrO_3$, thin films result in a measurable piezoresponse as a consequence of grain coalescence and reduction of free-charge accumulation. Here, the significant decrease in the electrical conductivity and the unsatured polarization may be related to the following factors: (i) all the $YCrO_3$ are coated with insulating Al_2O_3 showing homogeneous grain-insulating-grain contact in the ceramic matrix and (ii) the individual coating of $YCrO_3$ particles with Al_2O_3 shell results in barrier layers localizing the charge carriers at the $YCrO_3$ particles. These two important results, the decrease of the conductivity and the dielectric losses, can be ascribed to the alumina coating, and, as consequence, an unsaturated polarization hysteresis curve is observed. In addition, these results indicate that the primary source of spatial charges in $YCrO_3$ is on the surface and particles boundaries; these free charges carriers can be trapped by coating with insulating Al_2O_3 shells. Finally, it is clearly demonstrated that the core−shell design can be an alternative to decrease the electrical conductivity and allow the intrinsic hysteresis curve to appear, which is advantageous for practical applications.

CONCLUSIONS

Al_2O_3-coated multiferroic $YCrO_3$ ceramics were investigated in powders and bulk nanocomposites. The XRD and microstructural analyses suggest that the final nanocomposite array is composed of multiferroic particles covered with amorphous insulating Al_2O_3. Using the ALD technique, the thickness was readily controlled, producing continuous and homogeneous Al_2O_3 coating on the $YCrO_3$ particles. The Y@Al was subsequently annealed to consolidate the Al_2O_3 shell. Starting from the as-prepared ALD sample, the coercivity increased for 50 ALD cycles; after that, the coercive field was independent of the Al_2O_3-shell thickness. After heat treatment, the coercivity decreased and the magnetization increased as the Al_2O_3 thickness was increased. This behavior is ascribed to the exchange coupling through the Y@Al interface. The Al_2O_3 shell coated on the $YCrO_3$ particles serves as a barrier layer. This is due to the Al_2O_3 shell localizing the charge carriers and thus reducing the loss tangent and decreasing the electrical conductivity. The drastic decrease of the electric conductivity and the loss tangent makes the observation of the ferroelectric hysteresis loop at room temperature possible. The Y@Al array proves that the free charges at the grain boundaries are the main source that affects the hysteresis loops. These results show that the multiferroic properties can be improved by means of controlled layer growth of insulating Al_2O_3 shell in the bulk $YCrO_3$.

AUTHOR INFORMATION

Corresponding Author

*E-mail: dural@cnyn.unam.mx. Phone: ++52 (646) 174 46 02 ext 442. Fax: ++52 (646) 174 46 03.

Notes

The authors declare no competing financial interest.

ACKNOWLEDGMENTS

This work was supported by Universidad Nacional Autónoma de México (UNAM)-DGAPA, Project PAPIIT IN103213-3 and IN114209-3, IN106414; Consejo Nacional de Ciencia y Tecnología (CONaCyT), Project 166286 and 83275. R.E. thanks DGAPA-UNAM Project No. IN106014, CONACyT Project 129293 (Ciencia Básica), BISNANO, and Project PICCO 11-7 by The Institute of Sciences of Distrito Federal, Ciudad de México. We also thank R. Falconi, I. Gradilla, J. Peralta, F. Ruiz, A. Tiznado, and E. Medina for their technical support and O. E. Contreras for fruitful discussions.

REFERENCES

(1) Roy, R. *Mater. Sci. Res.* **1986**, *21*, 25−32.
(2) Komarneni, S. *J. Mater. Chem.* **1992**, *2*, 1219−1230.
(3) Sternitzke, M. *J. Eur. Ceram. Soc.* **1997**, *17*, 1061−1082.
(4) Niihara, K. *J. Ceram. Soc. Jpn.* **1991**, *99*, 974−982.
(5) Chakravorty, D. *Bull. Mater. Sci.* **1992**, *15*, 411−420.
(6) Caruso, F. *Adv. Mater.* **2001**, *13*, 11−22.
(7) Kundu, T. K.; Chakravorty, D. *Appl. Phys. Lett.* **1995**, *66*, 3576−3578.
(8) Martin, J. I.; Nogues, J.; Liu, K.; Schuller, I. K. *J. Magn. Magn. Mater.* **2003**, *256*, 449−501.
(9) Vestal, C. R.; Zhang, Z. J. *Nano Lett.* **2003**, *3*, 1739−43.
(10) Lee, J. Y.; Lee, J. H.; Hong, S. H.; Lee, Y. K.; Choi, J. Y. *Adv. Mater.* **2003**, *15*, 1655−8.
(11) Chung, U. C.; Elissalde, C.; Mornet, S.; Maglione, M. *Appl. Phys. Lett.* **2009**, *94*, 0729031−3.
(12) Li, S.; lin, Y. H.; Zhang, B. P.; Li, J. F.; Nan, C. W. *J. Appl. Phys.* **2009**, *105*, 054310−5.
(13) Chen, S. W.; Lee, C. C.; Chen, M. T.; Wu, J. M. *Nanotechnology* **2011**, *22*, 115605−5.
(14) Chung, U. C.; Elissalde, C.; Mompiou, F.; Majimel, J.; Gomez, S.; Estournes, C.; Marinel, S.; Klein, A.; Weill, F.; Michau, D.; Mornet, S.; Maglione, M. *J. Am. Ceram. Soc.* **2010**, *93*, 865−874.
(15) Durán, A.; Meza, C.; Carbajal-Arizaga, G. G. *Mater. Res. Bull.* **2012**, *47*, 1442−1447.
(16) Durán, A.; Arévalo-López, A. M.; Castillo-Martínez, E.; García-Guaderrama, M.; Morán, E.; Cruz, M. P.; Fernández, F.; Alario-Franco, M. A. *J. Solid State Chem.* **2010**, *183*, 1863−1867.

(17) Cruz, M. P.; Valdespino, D.; Gervacio, J. J.; Herrera, M.; Bueno-Baques, D.; Durán, A.; Muñoz, J.; Garcia-Castro, A. C.; Curiel, M.; Siqueiros, J. M. *Mater. Lett.* **2014**, *114*, 148−151.
(18) Robertson, J. *MRS Bull.* **2002**, *27*, 217−221.
(19) Robertson, J. *Rep. Prog. Phys.* **2006**, *69*, 327−396.
(20) Thornton, J. A.; Chin, J. *Am. Ceram. Soc. Bull.* **1977**, *56*, 504−508.
(21) Tiznado, H.; Domínguez, D.; de la Cruz, W.; Machorro, R.; Curiel, M.; Soto, G. *Rev. Mex. Fis.* **2012**, *58*, 459−465.
(22) Dameron, A. A.; Seghte, D.; Burton, B. B.; Davidson, S. D.; Cavanagh, A. S.; Bertrand, J. A.; George, S. M. *Chem. Mater.* **2008**, *20*, 3315−3326.
(23) Hoex, B.; Heil, S. B. S.; Langereis, E.; van de Sanden, M. C. M.; Kessels, W. M. M. *Appl. Phys. Lett.* **2006**, *89*, 042112−4.
(24) Ferguson, J. D.; Weimer, A. W.; George, S. M. *Thin Solid Films* **2000**, *371*, 95−104.
(25) Zhang, L.; Jiang, H. C.; Liu, C.; Dong, J. W.; Chow, P. *J. Phys. D: Appl. Phys.* **2007**, *40*, 3707−3713.
(26) Dilon, A. C.; Ott, A. W.; Way, J. D.; George, S. M. *Surf. Sci.* **1995**, *322*, 230−242.
(27) Groner, M. D.; Fabreguette, F. H.; Elam, J. W. *Chem. Mater.* **2004**, *16*, 639−645.
(28) Liang, X.; Li, N.-H.; Weiner, A. W. *Microporous Mesoporous Mater.* **2012**, *149*, 106−110.
(29) Cava, S.; Tebcherani, S. M.; Souza, I. A.; Pianaro, S. A.; Paskocimas, C. A.; Longo, E.; Varela, J. A. *Mater. Chem. Phys.* **2007**, *103*, 394−399.
(30) Kilbourn, B. T. *A Lanthanide Lanthology, a collection of notes concerning the lanthanides and related elements;* Molycorp, Inc.: Mountain Pass, CA, 1997.
(31) Subba Rao, G. B.; Wanklyn, B. M.; Rao, C. N. R. *J. Phys. Chem. Solids* **1971**, *32*, 345−358.
(32) Hakim, L. F.; King, D. M.; Zhou, Y.; Gump, C. J.; Steven, M. G.; Weime, A. W. *Adv. Funct. Mater.* **2007**, *17*, 3175−318.
(33) Jacobs, I. S.; Burne, H. F.; Levison, L. M. *J. Appl. Phys.* **1971**, *4*, 1631−2.
(34) Liu, W.; Zhong, W.; Jiang, H. Y.; Tang, N. J.; Wu, X. L.; Du, W. Y. *Eur. Phys. J. B* **2005**, *46*, 471−474.
(35) Zhao, Y.; Ni, C.; Kruczynski, D.; Zhang, X.; Xiao, J. Q. *J. Phys. Chem. B* **2004**, *108*, 3691−3693.
(36) Wu, M.; Zhang, Y. D.; Hui, S.; Xiao, T. D.; Ge, S.; Hines, W. A.; Budnick, J. I.; Yacaman, M. J. *Appl. Phys. Lett.* **2002**, *92*, 6809−6812.
(37) Banerjee, S.; Roy, S.; Chen, J. W.; Chakravorty, D. *J. Magn. Magn. Mater.* **2000**, *219*, 45−52.
(38) Leslie-Pelecky, D. L.; Rieke, R. D. *Chem. Mater.* **1996**, *8*, 1770−1783.
(39) Yang, G.; Gao, D.; Zhang, J.; Zhang, J.; Shi, Z.; Xue, D. *J. Phys. Chem. C* **2011**, *115*, 16814−16818.
(40) Sundaresan, A.; Rao, C. N. R. *Nano Today* **2009**, *4*, 96−106.
(41) Teague, J. R.; Gerson; James, W. J. *Solid State Commun.* **1970**, *8*, 1073−1074.
(42) Kim, J. K.; Kim, S. S.; Kim, W.-J.; Bhalla, A. S.; Guo, R. *Appl. Phys. Lett.* **2006**, *88*, 132901.
(43) Qi, X.; Dho, J.; Tomov, R.; Blamire, M. G.; MacManus-Driscoll, J. L. *Appl. Phys. Lett.* **2005**, *86*, 062903.
(44) Serrao, C. R.; Kundu, A. K.; Krupanidhi, S. B.; Waghmare, U. V.; Rao, C. N. R. *Phys. Rev. B: Condens. Matter. Mater. Phys.* **2005**, *72*, 220101(R).